Exploring Particle Based Modeling of Turbulent Multi-Phase Flow: A Comparative Study of SPH and MFM

M. Wicker, M. Okraschevski, R. Koch, H.-J. Bauer
Institute of Thermal Turbomachinery (ITS)
Karlsruhe Institute of Technology
Karlsruhe, Germany
markus.wicker@kit.edu

***Abstract*—For the numerical investigation of primary atomization, Smoothed Particle Hydrodynamics (SPH) is frequently employed due to its ability to capture extreme deformation of high-density-interfaces. The Meshless-Finite-Mass (MFM) method, another Lagrangian method that has emerged from the astrophysics community, promises to improve on the accuracy of SPH in turbulent flow applications such as primary atomization. In order to prepare MFM for the use in multi-phase engineering applications, a surface tension model is integrated into the open-source code *GIZMO* and validated against an oscillating droplet benchmark. A primary atomization benchmark is proposed and employed to compare the capabilities of MFM and SPH in turbulent multi-phase flow. It is established that the theoretical advantages of MFM indeed translate to a significant improvement of the benchmark results.**

I. Introduction

In the ongoing effort to reduce emissions of jet engines, fuel atomization is a key area of research as it is one that is not yet fully understood. The primary atomization of the fuel spray nozzles is characterized by high pressures and temperatures as well as a very dense spray. These conditions make experimental investigation highly expensive and complex, if not impossible. Consequently, numerical analysis is the method of choice. Due to its inherent ability to capture complex interfaces with high density ratios, Smoothed Particle Hydrodynamics (SPH) has proven to be a capable tool for this [1]–[4]. However, primary atomization is also characterized by a highly turbulent gas flow. The well-known issues of SPH in this area [5] give impetus towards further research.

Similar to the emergence of SPH, the Meshless-Finite-Mass method (MFM) has been gaining popularity in the astrophysics community. This method can be classified as a Lagrangian Finite-Volume method and promises to alleviate some of the drawbacks of SPH in turbulent applications. Critically, it does not exhibit the same zeroth-order convergence errors as SPH [6], [7]. As the use of MFM so far has been limited to the astrophysics community, the method lacks some necessary features for engineering applications. By virtue of the similarity between SPH and MFM though, models developed for the former can be transferred to the latter. Imperative is a surface tension model is needed to facilitate multi-phase simulations. As a first step, the commonly used surface tension model developed by Adami et al. [8] is implemented into the open source MFM code *GIZMO* [9]. A benchmark of an oscillating droplet is employed for this cross-method integration.

This adaptation of MFM enables for the first time a comparison with SPH in industrially relevant multi-phase flow applications. The enormous computational cost as well as the lack of other necessary features such as appropriate boundary conditions preclude a comparison of complete primary atomization simulations on similar scale as in [1]–[4]. Therefore, an analogon is needed. The Kelvin-Helmholtz instability is an ideal candidate for this, as it is one of the primary instabilities in air-blast atomization, as well as a commonly used benchmark case [9]–[12]. In order to comply with the limitations of the used MFM code, a numerical setup similar to the one described by Lecoanet et al. [10] is combined with a physical configuration akin to the liquid atomization as described by Chaussonnet et al. [3]. As a reference point, the MFM simulations are compared to results obtained with *turboSPH*, the same SPH code that was used in [1]–[4] and was specifically designed for application in this field. The resulting flow fields are compared and the influence of spatial resolution is discussed.

II. Numerical methods

A. Meshless-Finite-Mass method

MFM is a member of a class of Arbitrary Langrangian-Eulerian (ALE) mesh-free methods developed by Hopkins [9], [13], based on the work of Lanson and Vila [14], [15]. It is implemented in the open source code *GIZMO*, which is a highly modified version of *Gadget* [16]. It can be derived from the set of transport equations for mass, momentum and energy in an ALE reference frame:

$$\frac{\partial \vec{U}}{\partial t} + \vec{\nabla} \cdot (\boldsymbol{F} - \vec{u}_{\text{frame}} \otimes \vec{U}) = \vec{0}\,, \tag{1}$$

wherein $\vec{u}_{\text{frame}}$ is the frame velocity of the individual particles. The state vector $\vec{U}$ and the flux tensor $\boldsymbol{F}$ are given by

$$\vec{U} = \begin{pmatrix} \rho \\ \rho\vec{u} \\ \rho e \end{pmatrix}, \tag{2}$$

$$\boldsymbol{F} = \begin{pmatrix} \rho\vec{u} \\ \rho\vec{u} \otimes \vec{u} + p\boldsymbol{I} - \boldsymbol{\tau} \\ (\rho e + p)\vec{u} \end{pmatrix}. \tag{3}$$

Here, $\vec{u}$ denotes the velocity, e the total specific energy, p the pressure, $\boldsymbol{\tau}$ the shear stress tensor and $\boldsymbol{I}$ the identity tensor. Note that the energy equation is not solved in this work as only isothermal flows are considered. As MFM is a Lagrangian method, the frame velocity $\vec{u}_{\text{frame}}$ is set to the fluid velocity $\vec{u}$.

Unlike SPH, the kernel function W with its smoothing length h is not used as a smoothing function, but rather only as a way to discretize the domain. For every point $\vec{x}$ a volume fraction Ψ_i associated with a particle i is determined by

$$\psi_\text{i}(\vec{x}) = \frac{1}{\omega(\vec{x})} W(\vec{x} - \vec{x}_\text{i}, h) \,, \tag{4}$$

$$\omega(\vec{x}) = \sum_j W(\vec{x} - \vec{x}_\text{j}, h) \,. \tag{5}$$

The 'effective' volume of a particle i is then

$$V_\text{i} = \int \psi_\text{i}(\vec{x}) d\vec{x} \,. \tag{6}$$

Combined with a second-order accurate, locally centered least-squares matrix gradient estimator, this volume is used in a Galerkin-type approach to rewrite (1) as

$$\frac{d}{dt}(V_\text{i}\vec{U}_\text{i}) + \sum_j \tilde{\boldsymbol{F}}_\text{ij} \cdot \vec{A}_\text{ij} = \vec{0} \,. \tag{7}$$

It is important to note that A_ij is not a geometric face area but rather an 'effective face area' that is moving with a frame velocity such that mass is conserved on both sides of the face. The flux $\tilde{\boldsymbol{F}}_\text{ij}$ at the interface is the solution of a Riemann problem between particles i and j. This Riemann problem is solved employing an HLLC Riemann solver [17].

The set of equations is closed by the weekly-compressible equation of state introduced in [18]:

$$p - p_0 = \frac{\rho_0 a^2}{\gamma} \left[\left(\frac{\rho}{\rho_0} \right)^\gamma - 1 \right] \,, \tag{8}$$

with the thermodynamic pressure p and density ρ and their respective reference values denoted by the subscript '0', as well as the artificial speed of sound a and the polytropic ratio γ, which controls the compressibility effects.

B. Surface Tension Model

The surface tension model that is to be implemented must be able to handle interface density ratios in the order of hundreds. In such SPH calculations, the formulation presented by Adami et al. [8] has proven to be very reliable and is commonly employed. This formulation is a Continuum Surface Force model [19], in which the different phases are distinguished through a color function c. It introduces an additional term on the RHS of the momentum equation in the form of the volumetric surface tension force $\vec{F}_\sigma$

$$\vec{F}_\sigma = \sigma\kappa\vec{\nabla}c \tag{9}$$

with the surface tension σ and curvature κ. The color function c is defined as

$$c_l^k = \begin{cases} 1, & \text{if particles } k \text{ and } l \text{ are not of the same phase,} \\ 0, & \text{if particles } k \text{ and } l \text{ are of the same phase,} \end{cases} \tag{10}$$

and its gradient is determined by

$$\vec{\nabla}\hat{c}_\text{i} = \frac{1}{V_\text{i}} \sum_j [V_\text{i}^2 + V_\text{j}^2] \tilde{c}_\text{ij} \vec{\nabla} W_\text{ij} \,. \tag{11}$$

Here, $\vec{\nabla}W_\text{ij} = \vec{\nabla}W(\vec{x}_\text{i} - \vec{x}_\text{j}, h)$ is the shortened notation for the kernel gradient and $\tilde{c}_\text{ij}$ is the inter-particle density averaged color value:

$$\tilde{c}_\text{ij} = \frac{\rho_\text{j}}{\rho_\text{i} + \rho_\text{j}} c_\text{i}^\text{i} + \frac{\rho_\text{i}}{\rho_\text{i} + \rho_\text{j}} c_\text{j}^\text{i} \,. \tag{12}$$

The color gradient $\vec{\nabla}\hat{c}$ relates to the surface unit normal vector $\vec{\hat{n}}$ through

$$\vec{\hat{n}} = \frac{\vec{\nabla}\hat{c}(\vec{x})}{\|\vec{\nabla}\hat{c}(\vec{x})\|} \,, \tag{13}$$

which is in turn used to approximate the curvature κ_i at particle i using a reproducing divergence approximation with the number of dimensions d as

$$\kappa_\text{i} = -d \frac{\sum_j (\vec{\hat{n}}_\text{i} - \vec{\hat{n}}_\text{j}) \cdot \vec{\nabla} W_\text{ij} V_\text{j}}{\sum_j \|\vec{\nabla} W_\text{ij}\| V_\text{j}} \,. \tag{14}$$

C. SPH Scheme

For the reference computations the same SPH scheme as in [2] is employed as it has proven to be advantageous for primary atomization applications. The density is approximated using the discrete formulation introduced by Hu and Adams [20]:

$$\rho_\text{i} = m_\text{i} \sum_j W(\vec{x}_\text{i} - \vec{x}_\text{j}, h) \,, \tag{15}$$

with the shortened kernel notation $W_\text{ij} = W(\vec{x}_\text{i} - \vec{x}_\text{j}, h)$. The pressure gradient $\vec{\nabla}p_\text{a}$ is approximated by the formulation introduced in [21]

$$\vec{\nabla}p_\text{a} = \sum_j \frac{m_\text{j}}{\rho_\text{j}} (p_\text{i} + p_\text{j}) \vec{\nabla} W_\text{ij} \,. \tag{16}$$

The viscous force is realized as in [22]:

$$\vec{\nabla}\tau_\text{i} = \rho_\text{i} \sum_j 2m_\text{j} (d+2) \frac{\nu_\text{i} + \nu_\text{j}}{\rho_\text{i} + \rho_\text{j}} \frac{(\vec{u}_\text{i} - \vec{u}_\text{j}) \cdot \vec{r}_\text{ij}}{\|\vec{r}_\text{ij}\|^2 + 0.01h} \vec{\nabla} W_\text{ij} \,, \tag{17}$$

with the kinematic viscosity ν and the distance between two neighboring particles $\vec{r}_{ij}$

$$\vec{r}_{ij} = \vec{x}_i - \vec{x}_j \ . \tag{18}$$

III. Validation

A. Square droplet deformation

The implemented surface tension model is validated against a subset of the droplet benchmark from [8]. First, the deformation of an initially square droplet with the edge length $l_d = 0.6$ in a square domain with the edge length $L = 2$ under surface tension $\sigma = 1$ is predicted. The density of both fluids is set to $\rho_0 = 1$ with a dynamic viscosity $\mu = 0.05$. The domain is discretized using 3600 particles and a Wendland C4 kernel [23] with 32 neighbors, approximately equivalent to a ratio of smoothing length to particle spacing of $h/dx = 1.5$ [24]. The artificial speed of sound, background pressure and polytropic ratio are set to $a = 20$, $p_0 = 100$ and $\gamma = 1$, respectively. The particle arrangement and droplet shape are depicted in Fig. 1 for the initial state and once the equilibrium state is reached at $t_{eq} = 0.4$. Evidently, the model correctly predicts the circular equilibrium shape while maintaining a good particle order.

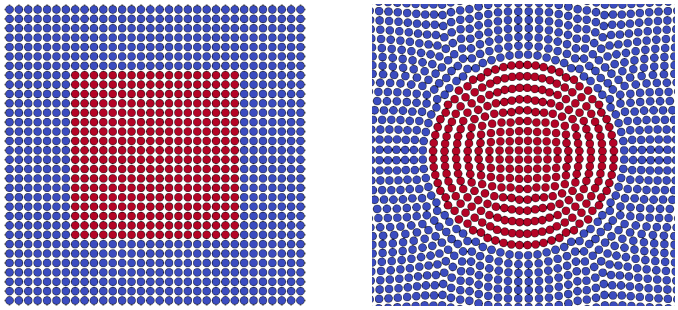

((a)) $t = 0$ ((b)) $t = t_{eq}$

Fig. 1: Droplet shape in the square droplet deformation case

B. Oscillating Droplet

In the second validation case, a circular droplet with a radius $r_d = 0.2$ is placed in a square domain with the edge length $L = 1$. The domain is discretized using 14400 particles ,and again the Wendland C4 kernel with $h/dx = 1.5$ is used. The droplet density and viscosity are once again set to $\rho_d = 1$ and $\mu_d = 0.05$, the density and viscosity ratio between the two fluids however are $\Phi = \rho_d/\rho_\infty = 1000$ and $\lambda = \mu_d/\mu_\infty = 100$. The background pressure is again set to $p_0 = 100$, and the polytropic ratio of the droplet and surrounding fluid to $\gamma_d = 7$ and $\gamma_\infty = 1$, respectively. The artificial speeds of sound are $a_d = 30$ and $a_\infty = 359$, following the impedance matching technique as described by Chaussonnet et al. [3]. The oscillation is induced by a prescribed initial droplet velocity field with $U_0 = 1$ and $r_0 = 0.05$:

$$U_x = U_0 \frac{x}{r_0} \left(1 - \frac{y^2}{r_0 r}\right) \exp\left(-\frac{r}{r_0}\right) \ , \tag{19}$$

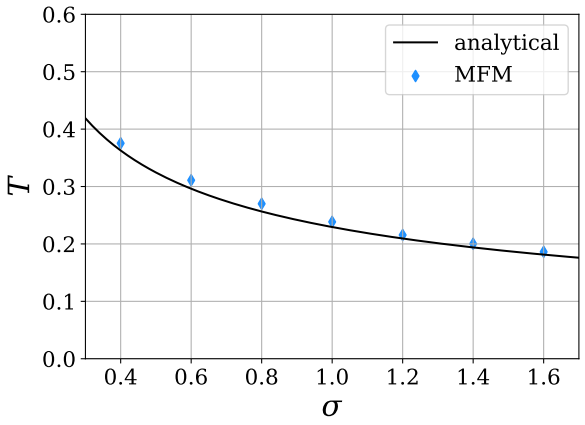

Fig. 2: Oscillation period T in the oscillating droplet case for varied surface tension values σ

$$U_y = -U_0 \frac{y}{r_0} \left(1 - \frac{x^2}{r_0 r}\right) \exp\left(-\frac{r}{r_0}\right) \ . \tag{20}$$

The relation between surface tension σ and oscillation period T is shown in Figure 2, along with the analytical solution

$$T_{th} = 2\pi \sqrt{\frac{r_d^3 \rho_d}{6\sigma}} \ . \tag{21}$$

The numerical results show excellent agreement with the analytical solution. As result of the validation, it is confirmed that surface tension model, which was originally developed for SPH integrates well into MFM.

IV. Kelvin-Helholtz instability

Upon demonstration of the correct integration of the surface tension model into MFM, the next step is a first assessment of the potential improvement that can be gained through the use of MFM in technically relevant multi-phase flows.

Comprehensive primary atomization simulations require an enormous amount of computational resources. Furthermore, accurate boundary conditions are of the utmost importance. As *GIZMO* lacks the latter and the former is impractical for this fundamental comparison, a simplified primary atomization benchmark is proposed. The Kelvin-Helmholtz instability is identified as the ideal candidate for this as it is both a common benchmark case as well as one of the primary instabilities in air-blast atomization.

A. Setup

The physical configuration is based on the work by Chaussonnet et al. [3] and the associated reference experiment [25]. The numerical configuration is similar to common benchmarks, such as [11] and [10]. A liquid jet with the diameter $d_l = 2\,\mathrm{mm}$ is placed laterally at the center of a in square or respectively cubic domain with the edge length $L = 4\,\mathrm{mm}$. The domain is discretized using N^d particles on a Cartesian lattice and the Wendland C4 kernel with smoothing length h. The fluid properties are given by $\rho_l = 1233\,\mathrm{kg/m^3}$ and $\mu_l =$

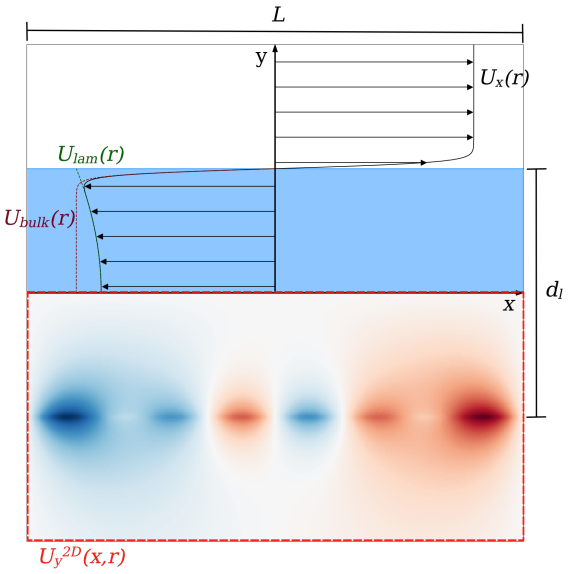

Fig. 3: Sketch of the initial velocity distribution U in the 2D Kelvin-Helmholtz instability case

0.2 Pas for the liquid, $\rho_g = 13.25\,\mathrm{kg/m^3}$ and $\mu_l = 18.61\,\mu$Pas for the gas, and the surface tension $\sigma = 63.6\,\mathrm{mN/m}$. The parameters in the equation of state for both fluids are $p_0 = 275\,\mathrm{kPa}$, $a_l = 150\,\mathrm{m/s}$, $\gamma_l = 7$, $a_g = 1450.9\,\mathrm{m/s}$ and $\gamma_g = 1$.

In [3], the mean gas velocity is $U_g = 58\,\mathrm{m/s}$ and the velocity of the liquid jet is $U_l = 0.55\,\mathrm{m/s}$. Here, the initial velocity in main flow direction as sketched in the upper half of Fig. 3 is given by:

$$U_x(r) = \begin{cases} U_{\text{bulk}}(r) + u_{\text{lam}}(r) & 0 \le r < d_l/2\,, \\ U_{\text{bulk}}(r) & d_l/2 \le r\,, \end{cases} \tag{22}$$

$$U_{\text{bulk}}(r) = (U_g + U_{\text{frame}}) \tanh\left(\frac{r - d_l/2}{\alpha}\right)\,, \tag{23}$$

$$U_{\text{lam}}(r) = 2U_l\left(1 - \frac{4r^2}{d_l^2}\right)\,, \tag{24}$$

with $\alpha = 5 \times 10^{-5}\,\mathrm{m}$. In 2D, the radial coordinate is $r = |y|$, and in 3D $r = \sqrt{y^2 + z^2}$. The frame velocity $U_{\text{frame}} = -\frac{1}{2}U_g$ is added to limit the necessary artificial speed of sound and thereby increase the time step size.

The instability is seeded through an initial superimposed sinusoidal velocity perturbation U_y, which in 2D simulations as visualized in the lower half of Fig. 3 is given by

$$U_y^{2D}(x,r) = \sum_{k=0}^{2} A \sin\left(\frac{2\pi}{\lambda_k}x\right) \exp\left(-\frac{2\pi}{\lambda_k}\left|\left(r - \frac{d_l}{2}\right)\right|\right)\,, \tag{25}$$

with the amplitude $A = 0.01\,U_g$.

In 3D simulations, a dependency on the tangential coordinate φ is added:

$$U_y^{3D}(x,r,\varphi) = \sum_{k=0}^{2} \sin\left(\frac{2\pi}{\lambda_k}\varphi\right) \cdot \sum_{k=0}^{2} A \sin\left(\frac{2\pi}{\lambda_k}x\right) \exp\left(-\frac{2\pi}{\lambda_k}\left|\left(r - \frac{d_l}{2}\right)\right|\right)\,. \tag{26}$$

The induced wave lengths are λ_k with the smallest wave length $\lambda_0 = L/4$:

$$\lambda_k = 2^k \lambda_0\,. \tag{27}$$

B. 2D Results

The fluid distributions resulting from the growing Kelvin-Helmholtz instability in 2D are shown in Fig. 4 for 3 separate instances in time. The baseline MFM computation with $N_1 = 200$ and $h_1 = 1.5dx$ is shown in Fig. 4a. At $t = 0.3\,\mathrm{ms}$, the jet surface exhibits one dominant primary wave and a minor secondary wave. As the instability continues to grow, the dominance of the primary wave is amplified and at $t = 0.6\,\mathrm{ms}$, solitary particles are stripped from its crest. Progressing from this, thin fluid ligaments protruding from the wave crest evolve. At $t = 2.0\,\mathrm{ms}$, these ligaments have been stretched to a point where they have started to disintegrate into solitary particles as well as some larger fragments.

Fig. 4b shows a comparative MFM simulation with $N_2 = 300$. As a consequence of this higher resolution, the instability growth is moderately increased with an apparent ligament development evident at $t = 0.6\,\mathrm{ms}$. Subsequently, the fluid distribution continues to evolve qualitatively very similar to the baseline result with the final distribution at $t = 2.0\,\mathrm{ms}$ exhibiting analogous ligaments. However, the disintegration results in a higher number of substantive fluid structures and less solitary particles compared to the baseline. This is a sign of convergence in primary atomization [26], illustrating MFM's favourable convergence properties independent of kernel radius.

The results from analogous SPH calculations are displayed in Fig. 4c and 4d. To start, the perturbations on the jet surface appear to be increased but more chaotic, and the secondary wave is more significant. After the initial stages, the evolution of fluid ligaments is impeded, resulting in shorter, more deformed structures compared to MFM. These observed differences are not significantly effected by the increased number of particles from 4c to 4d, although the ligaments that do evolve are moderately more delicate in the simulation with N_2^2 particles.

As formal convergence in SPH is, contrarily to MFM, dependent on the ratio of smoothing length to particle spacing, two additional computations with N_2^2 particles are performed and displayed in Figs. 4e and 4f with $h_2 = 2dx$ and $h_3 = 3dx$, respectively. In both simulations, an accelerated growth of the instability with less chaotic perturbation can be observed at $t = 0.3\,\mathrm{ms}$. For h_3 the fluid distribution at $t = 0.6\,\mathrm{ms}$ is, while still palpably different, more similar to the MFM simulation with N_2. This observation holds true for h_2, though to a lesser

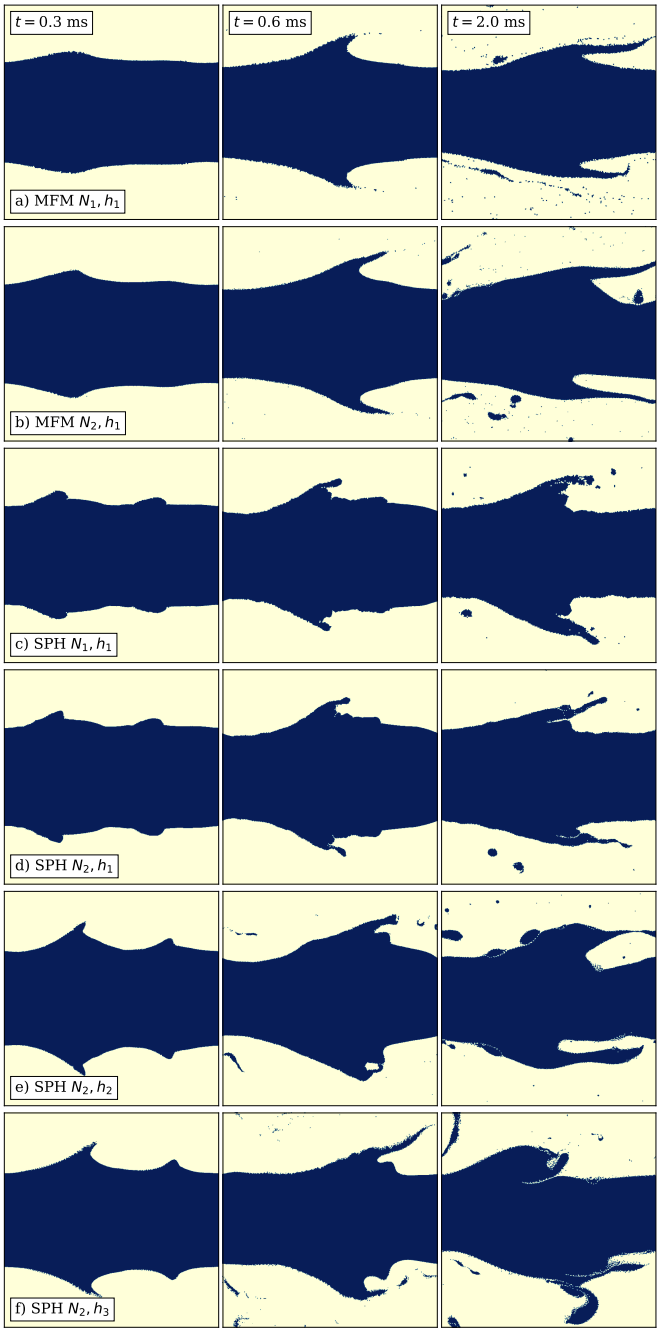

Fig. 4: Fluid distribution in the 2D Kelvin-Helmholtz instability benchmark for computations with MFM and SPH using varied number of particles N^2 and smoothing length h at 3 different times t

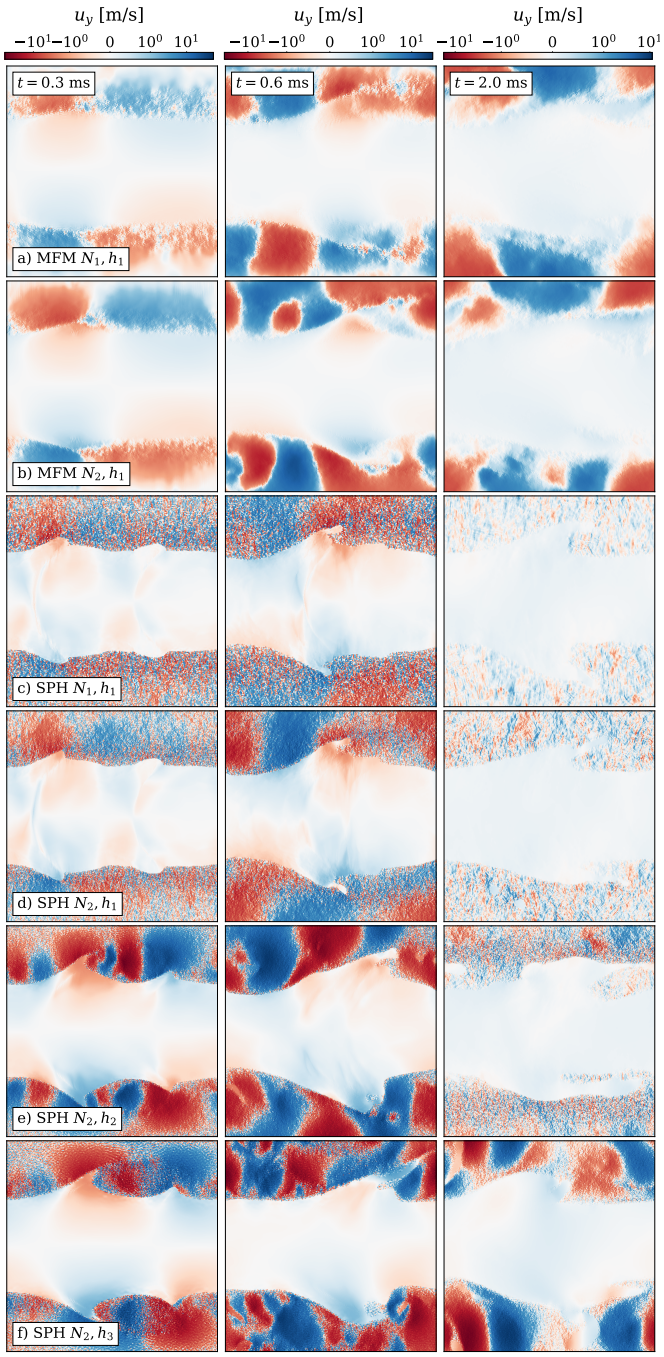

Fig. 5: Velocity component in y-direction in the 2D Kelvin-Helmholtz benchmark case for computations with MFM and SPH using varied number of particles N^2 and smoothing length h at 3 different times t

extent. The effect of the modified kernel is more pronounced at $t = 2.0\,\mathrm{ms}$. Here, the strongest similarity between MFM and SPH can be observed between Fig. 4b and 4e, even though the ligaments are still less delicate in the SPH results. The distribution in 4f on the other hand bears almost no resemblance to either MFM or SPH results obtained with h_1 or h_2.

In the pursuit of an explanation for the large differences between MFM and SPH results, an investigation into the behaviour of the gas phase is conducive. This is visualized in Fig. 5 through the y-velocity component u_y in the same simulations at the same time steps as in Fig. 4. Again, there is a strong similarity between the two MFM simulations in

Fig. 5a and 5b with slightly decreased noise for N_2. In comparison, the two SPH simulations with h_1 in Fig. 5c and 5d are characterized by a substantially higher level of noise, with again only a slight decrease with the higher number of particles. As a result of this noise, more turbulent kinetic energy is dissipated, resulting in a much lower magnitude of u_y at the final time $t = 2\,\mathrm{ms}$ compared to MFM. With increasing smoothing length in the simulations depicted in Fig. 5e and 5f the noise is decreased and consequently the magnitude of u_y increased.

With this observation, the shorter and less delicate fluid structures in the later stages of the first three SPH simulations can be explained by the higher dissipation of energy and less distinct vortices of the gaseous flow compared to the MFM results. The peculiar behaviour in Fig. 4f might be caused by a decreased 'effective resolution' due to the larger smoothing length h_3. As of now, the increased initial instability growth in SPH compared to MFM, particularly of the secondary instability, remains unexplained. Again this might be caused by the higher level of noise in the SPH simulations. Considering this, the physical validity of the increased growth is questionable.

C. 3D Results

In addition to the 2D simulations, the benchmark is computed in three dimensions using both SPH and MFM with N_1^3 particles and a Wendland C4 kernel with the smoothing length h_1. The resulting deformed liquid jets are displayed in Fig. 6. The different characteristics of MFM and SPH in this benchmark observed in 2D persist in 3D. Initially, at $t = 0.3\,\mathrm{ms}$, the SPH result exhibit an accelerated and more chaotic growth of the instability. At $t = 0.6\,\mathrm{ms}$, it can be observed that while the jet is still less perturbed for MFM, there is a thin membrane protruding from the crest of the dominant wave. Even though clusters with less than 10 liquid particles are excluded from display to increase visibility, the beginning of the disintegration is evident. In comparison, the fluid structures resulting from SPH are much less delicate.

Subsequently, the level of chaos increases while the general differences between SPH and MFM persist. The MFM result exhibits elongated membranes and ligaments that disintegrate at the edges at $t = 1.0\,\mathrm{ms}$. In SPH in comparison, the waves continue to grow further in the radial direction, while the development of elongated structures parallel to the bulk flow is much less pronounced. At the end of the simulation at $t = 2.0\,\mathrm{ms}$, both cases show a substantial number of larger droplets stripped away from the bulk jet. In MFM, these droplets are results of the disintegration of ligaments which in turn develop from membranes. In the case of the SPH simulation, fewer droplets are formed from shorter ligaments and the development of membranes is almost non-existent. Overall, these 3D simulations confirm the observations made in 2D excellently.

V. Conclusion

In this work, a surface tension model was integrated and validated in a Meshless-Finite-Mass code . Thereby it was

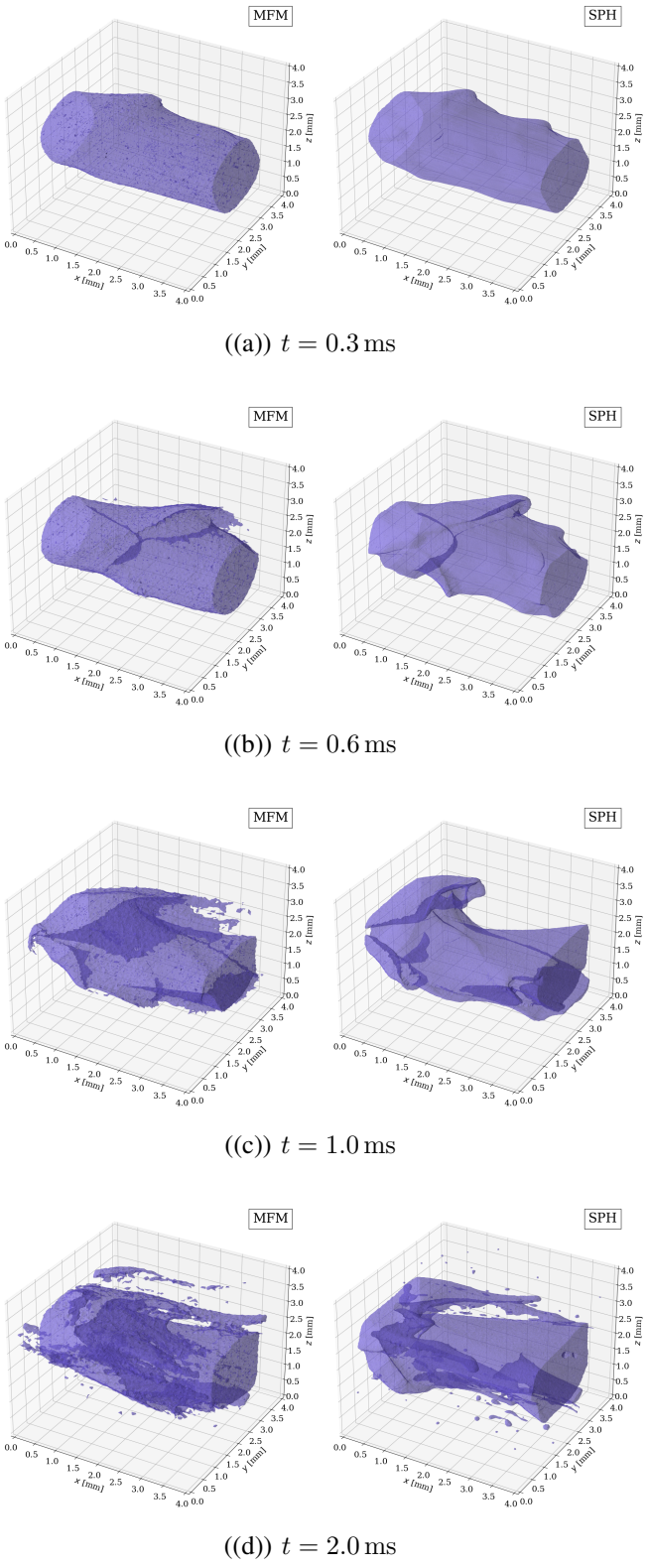

((a)) $t = 0.3\,\mathrm{ms}$

((b)) $t = 0.6\,\mathrm{ms}$

((c)) $t = 1.0\,\mathrm{ms}$

((d)) $t = 2.0\,\mathrm{ms}$

Fig. 6: 3D liquid jet computed using MFM and SPH with N_1^3 particles and smoothing length h_1

proven that through the inclusion of SPH models, MFM might be a viable alternative for the numerical analysis of engineering applications. Furthermore, this facilitated a first-time comparison of MFM and SPH in technically relevant multi-phase flows.

For further analysis, a Kelvin-Helmholtz configuration resembling primary atomization was proposed. The difference in the behaviour of the two methods in this benchmark case is apparent. The MFM results exhibit enhanced evolution of long, thin fluid structures and reduced small scale noise in the velocity field. While MFM reacts predictably and favourably to an increase of the number of particles, the assessment of the spatial resolution of the SPH simulations is ambiguous. A conclusive evaluation of which combination of particle number and kernel size performed best is not possible.

Even though these differences are evident, their classification is troublesome. Due to the simplified nature of the setup with its periodic boundaries, the instability growth deviates significantly from the behaviour established in literature [3], [25]. Therefore, a critical examination of the applicability to realistic problems must follow. First, the observations of the early stages of the instability growth cannot simply be transferred to more complex multi-phase problems, in which instabilities are not artificially seeded but rather induced through chaotic perturbation of the interface. Second, while MFM leads to enhanced development of very delicate fluid structures, the significance to reality is uncertain. It is to be expected, that membranes as they can be seen on the left hand side in Figs. 6(c) and 6(d) would disintegrate at a much earlier state compared to the structures present in the SPH result. Finally, the impact of excessive dissipation due to small scale velocity noise is amplified in the periodic boundary box compared to setups where momentum flux over the domain boundary is considered.

Even considering these uncertainties, this work clearly shows that in multi-phase applications where SPH is used due to its inherent ability to capture complex interface deformation, MFM has the potential to improve accuracy of numerical analysis if turbulence is a factor.

ACKNOWLEDGMENT

The authors acknowledge support by the state of Baden-Württemberg through bwHPC.

REFERENCES

[1] R. Koch, S. Braun, L. Wieth, G. Chaussonnet, T. Dauch, and H.-J. Bauer, "Prediction of primary atomization using smoothed particle hydrodynamics," *European Journal of Mechanics - B/Fluids*, vol. 61, pp. 271–278, 2017.

[2] S. Braun, L. Wieth, S. Holz, T. F. Dauch, M. C. Keller, G. Chaussonnet, S. Gepperth, R. Koch, and H.-J. Bauer, "Numerical prediction of air-assisted primary atomization using smoothed particle hydrodynamics," *International Journal of Multiphase Flow*, vol. 114, pp. 303–315, 2019.

[3] G. Chaussonnet, S. Braun, T. Dauch, M. Keller, A. Sänger, T. Jakobs, R. Koch, T. Kolb, and H.-J. Bauer, "Toward the development of a virtual spray test-rig using the smoothed particle hydrodynamics method," *Computers & Fluids*, vol. 180, pp. 68–81, 2019.

[4] T. F. Dauch, G. Chaussonnet, M. C. Keller, M. Okraschevski, C. Ates, R. Koch, and H.-J. Bauer, "3d predictions of the primary breakup of fuel in spray nozzles for aero engines," in *High Performance Computing in Science and Engineering '20*, W. E. Nagel, D. H. Kröner, and M. M. Resch, Eds. Cham: Springer International Publishing, 2021, pp. 419–433.

[5] A. Bauer and V. Springel, "Subsonic turbulence in smoothed particle hydrodynamics and moving-mesh simulations," *Monthly Notices of the Royal Astronomical Society*, vol. 423, no. 3, pp. 2558–2578, 2012.

[6] J. I. Read, T. Hayfield, and O. Agertz, "Resolving mixing in smoothed particle hydrodynamics," *Monthly Notices of the Royal Astronomical Society*, pp. no–no, 2010.

[7] Q. Zhu, L. Hernquist, and Y. Li, "Numerical convergence in smoothed particle hydrodynamics," *The Astrophysical Journal*, vol. 800, no. 1, p. 6, 2015.

[8] S. Adami, X. Y. Hu, and N. A. Adams, "A new surface-tension formulation for multi-phase sph using a reproducing divergence approximation," *Journal of Computational Physics*, vol. 229, no. 13, pp. 5011–5021, 2010.

[9] P. F. Hopkins, "A new class of accurate, mesh-free hydrodynamic simulation methods," *Monthly Notices of the Royal Astronomical Society*, vol. 450, no. 1, pp. 53–110, 2015.

[10] D. Lecoanet, M. McCourt, E. Quataert, K. J. Burns, G. M. Vasil, J. S. Oishi, B. P. Brown, J. M. Stone, and R. M. O'Leary, "A validated non-linear kelvin–helmholtz benchmark for numerical hydrodynamics," *Monthly Notices of the Royal Astronomical Society*, vol. 455, no. 4, pp. 4274–4288, 2016.

[11] C. P. McNally, W. Lyra, and J.-C. Passy, "A well-posed kelvin-helmholtz instability test and comparison," *The Astrophysical Journal Supplement Series*, vol. 201, no. 2, p. 18, 2012.

[12] T. S. Tricco, "The kelvin–helmholtz instability and smoothed particle hydrodynamics," *Monthly Notices of the Royal Astronomical Society*, vol. 488, no. 4, pp. 5210–5224, 2019.

[13] P. F. Hopkins, "Anisotropic diffusion in mesh-free numerical magnetohydrodynamics," *Monthly Notices of the Royal Astronomical Society*, vol. 466, no. 3, pp. 3387–3405, 2017.

[14] N. Lanson and J.-P. Vila, "Renormalized meshfree schemes i: Consistency, stability, and hybrid methods for conservation laws," *SIAM Journal on Numerical Analysis*, vol. 46, no. 4, pp. 1912–1934, 2008.

[15] ——, "Renormalized meshfree schemes ii: Convergence for scalar conservation laws," *SIAM Journal on Numerical Analysis*, vol. 46, no. 4, pp. 1935–1964, 2008.

[16] V. Springel, "The cosmological simulation code gadget-2," *Monthly Notices of the Royal Astronomical Society*, vol. 364, no. 4, pp. 1105–1134, 2005.

[17] E. F. Toro, "The hllc riemann solver," *Shock Waves*, vol. 29, no. 8, pp. 1065–1082, 2019.

[18] R. H. Cole and R. Weller, "Underwater explosions," *Physics Today*, vol. 1, no. 6, p. 35, 1948.

[19] J. Brackbill, D. Kothe, and C. Zemach, "A continuum method for modeling surface tension," *Journal of Computational Physics*, vol. 100, no. 2, pp. 335–354, 1992.

[20] X. Y. Hu and N. A. Adams, "A multi-phase sph method for macroscopic and mesoscopic flows," *Journal of Computational Physics*, vol. 213, no. 2, pp. 844–861, 2006.

[21] A. Colagrossi and M. Landrini, "Numerical simulation of interfacial flows by smoothed particle hydrodynamics," *Journal of Computational Physics*, vol. 191, no. 2, pp. 448–475, 2003.

[22] K. Szewc, J. Pozorski, and J.-P. Minier, "Analysis of the incompressibility constraint in the smoothed particle hydrodynamics method," *International Journal for Numerical Methods in Engineering*, vol. 92, no. 4, pp. 343–369, 2012.

[23] H. Wendland, "Piecewise polynomial, positive definite and compactly supported radial functions of minimal degree," *Advances in Computational Mathematics*, vol. 4, no. 1, pp. 389–396, 1995.

[24] W. Dehnen and H. Aly, "Improving convergence in smoothed particle hydrodynamics simulations without pairing instability," *Monthly Notices of the Royal Astronomical Society*, vol. 425, no. 2, pp. 1068–1082, 2012.

[25] A. Sänger, T. Jakobs, N. Djordjevic, and T. Kolb, "Effect of primary instability of a high viscous liquid jet on the spray quality generated by a twin-fluid atomizer," in *26th European Conference Liquid Atomization and Spray Systems*, L. Achelis, Ed., Bremen, 2014.

[26] S. Braun, S. Holz, L. Wieth, T. F. Dauch, M. C. Keller, G. Chaussonnet, C. Schwitzke, and H.-J. Bauer, "Hpc predictions of primary atomization with sph : Validation and comparison to experimental results," in *12th International SPHERIC Workshop, Ourense, E, J*, 2017.